PLOS ONE

RESEARCH ARTICLE

Efficient visible light photocatalysis of benzene, toluene, ethylbenzene and xylene (BTEX) in aqueous solutions using supported zinc oxide nanorods

Jamal Al-Sabahi[1,2], Tanujjal Bora[3], Mohammed Al-Abri[1,2]*, Joydeep Dutta[4]*

1 Department of Petroleum and Chemical Engineering, College of Engineering, Sultan Qaboos University, Al-Khoudh, Oman, **2** Chair in Nanotechnology for Water Desalination, Water Research Center, Sultan Qaboos University, Al-Khoudh, Oman, **3** Center of Excellence in Nanotechnology, Asian Institute of Technology, Klong Luang, Pathumthani, Thailand, **4** Functional Materials, Department of Applied Physics, School of Engineering Sciences, KTH Royal Institute of Technology, Kista, Stockholm, Sweden

* alabri@squ.edu.om (MA); joydeep@kth.se (JD)

Citation: Al-Sabahi J, Bora T, Al-Abri M, Dutta J (2017) Efficient visible light photocatalysis of benzene, toluene, ethylbenzene and xylene (BTEX) in aqueous solutions using supported zinc oxide nanorods. PLoS ONE 12(12): e0189276. https://doi.org/10.1371/journal.pone.0189276

Editor: Yogendra Kumar Mishra, Institute of Materials Science, GERMANY

Received: July 18, 2017

Accepted: November 22, 2017

Published: December 20, 2017

Data Availability Statement: All relevant data are within the paper and its Supporting Information files.

Funding: This work was supported by The Research Center (TRC) represented by the Chair in Nanotechnology Sultanate of Oman.

Competing interests: The authors have declared that no competing interests exist.

Abstract

Benzene, toluene, ethylbenzene and xylenes (BTEX) are some of the common environmental pollutants originating mainly from oil and gas industries, which are toxic to human as well as other living organisms in the ecosystem. Here we investigate photocatalytic degradation of BTEX under visible light irradiation using supported zinc oxide (ZnO) nanorods grown on glass substrates using a microwave assisted hydrothermal method. ZnO nanorods were characterized by electron microscopy, X-ray diffraction (XRD), specific surface area, UV/visible absorption and photoluminescence spectroscopy. Visible light photocatalytic degradation products of BTEX are studied for individual components using gas chromatograph/mass spectrometer (GC/MS). ZnO nanorods with significant amount of electronic defect states, due to the fast crystallization of the nanorods under microwave irradiation, exhibited efficient degradation of BTEX under visible light, degrading more than 80% of the individual BTEX components in 180 minutes. Effect of initial concentration of BTEX as individual components is also probed and the photocatalytic activity of the ZnO nanorods in different conditions is explored. Formation of intermediate byproducts such as phenol, benzyl alcohol, benzaldehyde and benzoic acid were confirmed by our HPLC analysis which could be due to the photocatalytic degradation of BTEX. Carbon dioxide was evaluated and showed an increasing pattern over time indicating the mineralization process confirming the conversion of toxic organic compounds into benign products.

Introduction

Petroleum industries are contributing largely in the global economy as well as in the development of oil-producing countries. Millions of barrels of crude oil are produced worldwide every day, which contains potentially toxic chemicals used in drilling, as well as natural

contaminants ejected from the oil wells, including total dissolved solids (e.g., salts, barium, strontium), organic compounds (mainly aliphatic and aromatic hydrocarbons) and normally occurring radioactive material (NORM), such as Radium 226 [1–4]. Aromatic hydrocarbons in crude oil is composed of trace amounts of polycyclic aromatic hydrocarbons (PAHs) that are relatively less soluble in water and high concentrations of monoaromatic hydrocarbons such as benzene, toluene, ethylbenzene and xylenes (BTEX) that are grouped as volatile organic compounds (VOCs), some of which are relatively soluble in water. Both groups contribute to environmental contamination when released into the environment finding their way to water, soil and air [5]. Benzene, toluene, ethylbenzene, and xylene (i.e., BTEX), though present in low percentages in crude oil are of high interest as they have been associated with adverse human health effects [6]. Produced water from oilfields and refinery wastewater usually contain some amounts of monoaromatic hydrocarbons as well [7–9]. Lined holding ponds that are constructed at well sites for temporary storage of the produced water are potential sources of surface spills and leaks of BTEX-containing liquids and also have the potential to leak into aquifers due to structural failure of casings and/or stray gas migrations [10]. Benzene can threaten human health and is mutagenic and carcinogenic [5]. It has a high vapor pressure that can rapidly contaminate the surrounding air, which can then lead to water and soil contamination via rainfall. Other BTEX compounds are derivatives of benzene which also show toxic effects. Benzene (5 ppb), toluene (1000 ppb), ethylbenzene (700 ppb) and xylene (10,000 ppb) are the permissible limits of drinking water maximum contaminant level (MCL) [11].

Different treatment technologies are in use for BTEX removal, such as biological treatment, chemical adsorption and advanced oxidation processes (AOPs) [12–16]. Among these, AOPs are a cluster of processes that produce high reactive hydroxyl radicals ($OH^{\bullet}$) leading to the destruction of harmful organic contaminants present in test matrix [17–19]. Photocatalysis is one of the popular AOPs for converting organic pollutants into harmless products, like CO_2, H_2O and mineral acids [20,21]. Furthermore, it is cost-effective, safe, non-selective and compatible to treat a broad range of organic contaminants [22–24]. Semiconductor photocatalysis lead to the mineralization of organic pollutants when it is irradiated with ultraviolet (UV) or visible light [25]. Carbon nanotubes (CNTs) also have been reported as an active nanomaterial for photocatalytic degradation of toxic organic contaminants and for sensing of heavy metals such as chromium and aluminum (III) ions in water [26–28]. Zinc oxide (ZnO), titanium dioxide (TiO_2) and tin dioxide (SnO_2) are the most widely used wide bandgap semiconductor photocatalysts [29,30]. The use of UV lamps is expensive and not practical for large area applications. Sunlight in retrospect, can be a viable cost-effective solution for large scale use of photocatalysis for the degradation of organic matters, but it contains only about 5% UV and 45% visible light [31]. Since ZnO is a wide bandgap semiconductor, modification of the material is necessary to make it visible light active in order to harvest major part of the solar spectra. Many studies are available in the literature offering different strategies to render ZnO materials visible light active. For example, coupling of ZnO with plasmonic metals [32,33], metal and non-metal doping [34,35], composites with another semiconductors [36–39], and self-doping by inducing crystal defects [40–44].

Nanotechnological application using zinc oxide nanomaterial got much respective attention and particularly in medical investigation and its applications, photocatalysis and material science. Zinc oxide is applied as anticancer agents [45,46]. Zinc oxide is widely used for photocatalytic degradation of toxic contaminants in water [47–50]. It is also used as antibacterial activity and antifouling [51,52], gas sensing [49,53] and for flame transport approach [48,54].

Photocatalytic degradation of BTEX, whether individually or as a group, in gaseous samples using UV light have been intensively studied, while very little research has been done to

investigate BTEX degradation in aqueous solutions and that too with visible light [55–57]. Toluene was reported to be more degradable than benzene when visible light photocatalysis is used for aqueous solution [57]. Although BTEX is volatile, its presence is always detected in the wastewater produced typically in oil and gas industries. In the present study, we therefore probe the photocatalytic degradation of BTEX in aqueous medium using visible light active defect engineered ZnO nanorods [58]. ZnO nanorods were hydrothermally grown on microscopic glass substrates and used as supported photocatalyst. Degradation of BTEX in aqueous solution as individual components was then investigated and discussed. Intermediate formation of byproducts was also evaluated using a mixed BTEX solution and evolution of carbon dioxide as a result of complete mineralization of BTEX was probed by gas chromatograph equipped with thermal conductivity detector (TCD).

Materials and methods

Synthesis of zinc oxide nanorods

Microwave assisted hydrothermal (MAH) process for the synthesis of ZnO nanorods is discussed in our previous reports [41,58,59]. Microscope glass substrates were successively cleaned with soap water, ethanol, acetone and finally with deionized (DI) water in an ultrasonic water bath for 15 minutes respectively. The clean glass substrates were then placed on a hotplate at 350˚C and a ZnO seed layer was deposited on them by direct spraying of 10 mM zinc acetate dihydrate [$Zn(CH_3COO)_2.2H_2O$; Merck] aqueous solution. The ZnO seeded glass substrates were then dipped in an aqueous solution comprising of 20 mM zinc nitrate hexahydrate [$Zn(NO_3)_2{\cdot}6H_2O$; Sigma] and 20 mM hexamethylenetetramine (HMTA; Merck). The reaction vessel was then heated in a commercial microwave oven (Samsung model# ME731K, serial # J68C7WFC5015084Y) operated at 180 W (growth solution temperature: 90˚C) for 45 minutes and then allowed to cool down naturally for 15 minutes [58]. The growth solution was then replenished with a fresh solution and the heating process was continued for another 4 similar cycles [60]. After the 5th cycle of microwave treatment, the glass substrates were removed, rinsed with DI water and dried in an oven at 90˚C. The as prepared ZnO nanorod coated glass substrates were then annealed at 350˚C in air for 1 hour in order to improve the visible light photocatalytic (VLP) activity of the nanorods. The annealing temperature was fixed based on our previous results where we have shown that the VLP activity of the ZnO nanorods can be improved through temperature induced defect migration from the bulk to the surface of ZnO nanorods [41].

ZnO nanorod characterization

Scanning electron microscopy (SEM, JEOL JSM-7600F) operated at 20 kV was used to investigate the morphology of the synthesized ZnO nanorods. X-ray diffraction technique (XRD, Rigaku miniflex 600) with Cu Kα radiation ($\lambda = 0.154$ nm) was used to study the crystal structure of the nanorods. XRD pattern was recorded in the 2θ range from 20˚ to 80˚ in 0.02˚/s steps. The specific surface area was determined using nuclear magnetic resonance (NMR) technology from Xigo Nanotools. Field emission transmission electron microscope (TEM, JEOL JEM-2100F) was used for the morphological structure, crystal nature and the lattice fringe spacing. A double beam UV-visible spectrometer (Perkin Elmer Lambda 25) was used to measure the steady state optical absorption spectrum of the ZnO nanorods. Photoluminescence (PL) spectra were collected at room temperature using a fluorescence spectrometer (Perkin Elmer LS 55). ZnO nanorods were excited with 325 nm monochromatic wavelength in order to obtain PL spectra at ambient conditions.

Photocatalytic degradation tests for BTEX

An aqueous benzene solution (10 ppm) was prepared and a 25-ml sealed glass bottle was filled with the benzene solution following which the bottle was sealed with a septum cap. Prior to the sealing, a ZnO nanorod coated glass slide (dimensions of 4 cm x 1.25 cm) was placed vertically in the bottle. The sealed bottle was then stored in dark at room temperature for 2 hours in order to obtain equilibrium between the benzene molecules adsorption and desorption at the ZnO surface. After 2 hours, the bottle was illuminated with artificial solar irradiation (incident power: 1 kW/m^2) using a Sciencetech solar simulator (SS1.6 kW). Another similar sealed glass bottle filled with 10 ppm benzene aqueous solution in the absence of any photocatalyst was used under similar conditions as control sample. Photocatalytic degradation of benzene was continued up to 3 hours and at regular intervals 300 μl of benzene aliquots were collected with a syringe to analyze the reduction in benzene concentration due to the photocatalytic reactions. Similar steps were applied for photocatalytic degradation of toluene, ethylbenzene and xylene under visible light irradiation. The initial concentration of the test contaminants was then varied from 10 to 100 ppm by keeping all the other parameters same in order to investigate the effect of initial concentration of the contaminants on the kinetics of the photocatalytic reactions. Degradation kinetics was studied by analyzing the VOC contents using gas chromatograph-mass spectrometer (GC/MS) technique. A mixture of BTEX solution (25 ppm) was also used to test for intermediate byproduct formation and carbon dioxide evolution during the photocatalytic degradation of BTEX. The experimental details were illustrated (Fig 1).

Analytical methods

Photocatalytic reduction of BTEX with time was monitored by gas chromatograph equipped with mass spectrometer (GC/MS, Shimadzu model# QP2010 Ultra) along with an autosampler

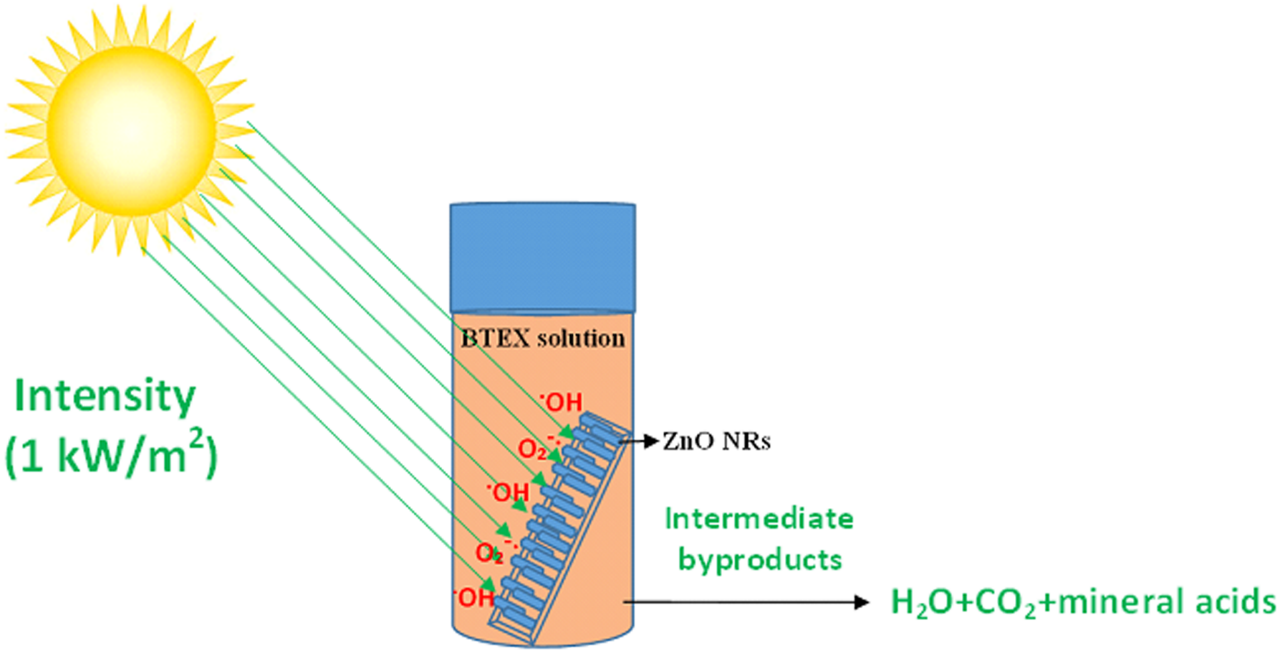

Fig 1. Schematic representation of a photocatalytic process using zinc oxide nanorods for degrading the monoaromatic hydrocarbons.

https://doi.org/10.1371/journal.pone.0189276.g001

(Shimadzu model# AOC-20i) injecting 1 μl sample into the GC. A polar capillary column (Rtx-Wax, 30 m length, 0.25 mm I.D., 0.25 μm film thicknesses, Restek) was used for BTEX analysis. High purity helium was used as the carrier gas (99.9999%) with a flow rate of 1 ml/min. The injector, MS interface and ion source temperatures were 250, 250 and 220˚C, respectively. The initial oven temperature was set at 60˚C and increased to 150˚C by slowly heating at 6˚C/min (15 minutes run time). The mass-spectroscopic (MS) fragments were scanned in 35–300 amu. Spectral library (NIST14 database) was used to identify the compounds of interest. All results were then plotted as C_t/C_o against time t, where C_t represents concentration of each monoaromatic hydrocarbon at a given time interval and C_o represents their starting concentration.

The intermediate products formed during photocatalysis were evaluated by high performance liquid chromatography (HPLC) equipped with an autosampler (SIL-30A, Shimadzu, Tokyo, Japan) and an ODS hypersil column (particle size: 3 μm, internal diameter: 4.6 mm, length: 80 mm) from Hewlett Packard, Santa Clara, CA, USA. The mobile phase was prepared by mixing water and methanol in a ratio 50:50 and was degassed before use. The flow rate of the mobile phase was 0.6 mL/min. 20 μl of samples were injected into the system each time and the sample was scanned from 200 to 400 nm to probe the intermediates using a photodiode array detector (SPD-M20A) from Shimadzu, Japan.

For detecting the carbon dioxide evolved as a result of complete mineralization of BTEX, gas chromatograph with thermal conductivity detector (Agilent 6890N) was used. 250 μl of the headspace gas, using gas-tight syringe, was injected every 30 minutes into a HP-PLOT Q column (HP-PLOT Q, 30 m length, 0.53 mm internal diameter, 40 μm film thicknesses, J&W Scientific). The set flow rate of helium (99.9995%) was 4 ml/min in a split mode (split ratio 10:1). The temperatures of the injection port and the detector were kept at 200˚C and 210˚C, respectively. The initial oven temperature was set at 50˚C and slowly increased to 80˚C (holding for 3 minutes) at a rate of 20˚C/min. The total run time was 4.5 minutes.

Results and discussion

The morphology of the as prepared ZnO nanorods was studied using scanning electron microscope (SEM) and vertically aligned ZnO nanorods growing from the glass substrates could be observed, as shown in Fig 2(a). The ZnO nanorods have an average length of about 4.5 μm as shown in the inset, with the characteristic hexagonal shape of ZnO nanorods being evident with an average diameter of about 100 nm. Fig 2(b) shows the XRD pattern of the ZnO nanorods where the diffraction peaks conform to the hexagonal crystal structure of ZnO nanorods as confirmed with the Joint Committee on Powder Diffraction Standards (JCPDS card# 01-070-8070). The preferential orientation of the ZnO nanorods along the (002) crystal plane is indicated by the strongest XRD peak at θ = 34.35˚C representing the (002) plane of the wurtzite crystal structure [61,62]. The specific surface area of the synthesized zinc oxide nanorods was determined by using Xigo nanotools system that works based on NMR technique and found to be 4.2 ± 0.5 m^2/g.

Fig 3 reveals that the low resolution TEM micrograph confirming the structural formation of ZnO nanorods where the diameter is about 100 nm. The clear lattice fringe spacing (d-spacing) is 0.26 nm confirming the hexagonal wurtzite structure and the presence of the dominant (002) plane [63] was detected. The selected area electron diffraction (SAED) pattern is assuring a single crystal formation of ZnO nanorods [64], synthesized by MAH process, as was observed using high resolution TEM (HRTEM).

Fig 4(a) shows the UV/Visible optical absorption spectra of the zinc oxide nanorod coated substrates. The nanorods exhibit strong absorption above 385 nm and show an extension of

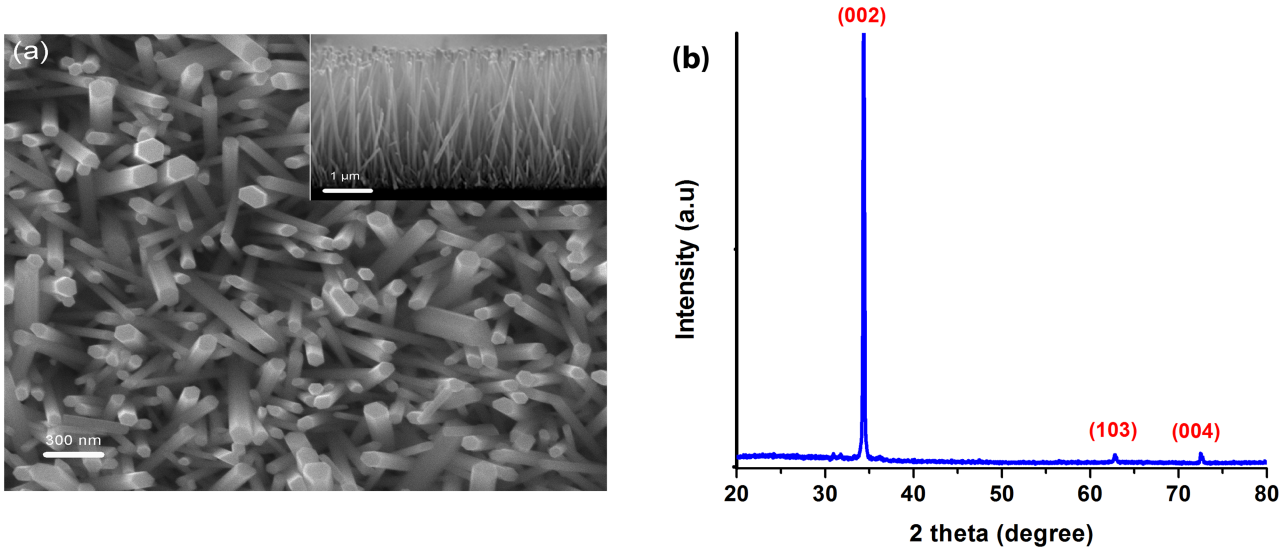

Fig 2. (a) Top and cross-sectional (inset) SEM micrographs and (b) XRD pattern of ZnO nanorods. (a) SEM micrographs of ZnO nanorods and (b) XRD pattern of the microwave assisted hydrothermally grown ZnO nanorods on glass substrate. Samples were annealed at 350˚C for 1 h after the hydrothermal growth.

https://doi.org/10.1371/journal.pone.0189276.g002

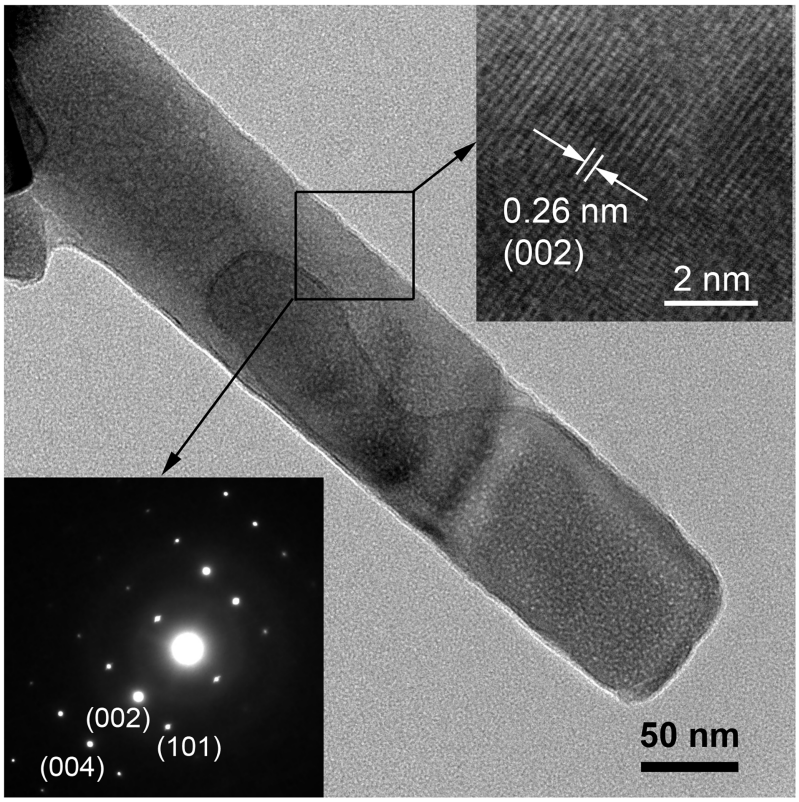

Fig 3. TEM micrograph of a synthesized single nanorod. The top inset representing the lattice fringes in the ZnO nanorods and the bottom inset is for the high resolution TEM showing the SAED pattern.

https://doi.org/10.1371/journal.pone.0189276.g003

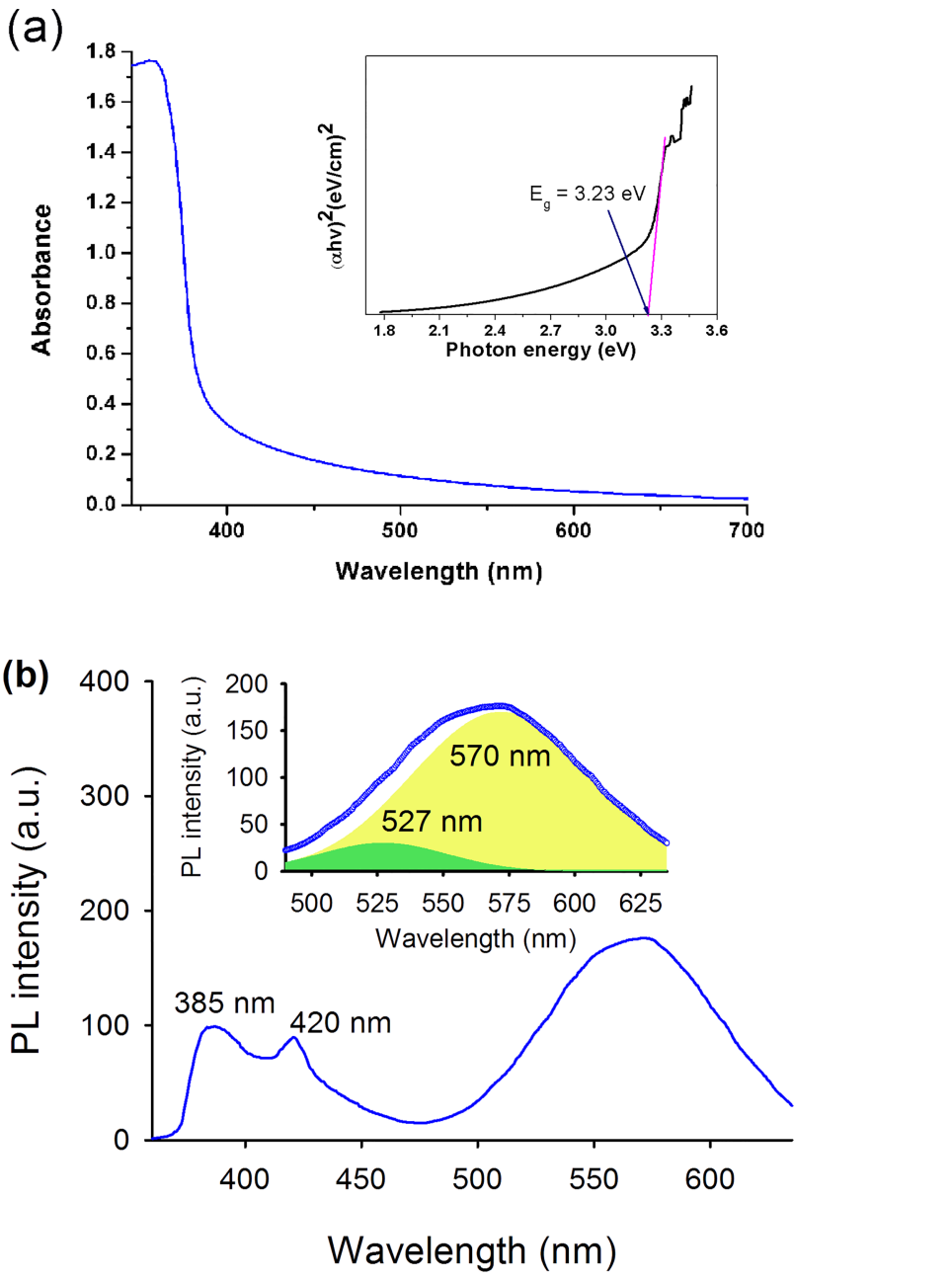

Fig 4. (a) Typical optical absorption spectrum and (b) room temperature photoluminescence (PL) spectrum of ZnO nanorods. Inset in Fig 4a representing the tauc plot and inset in Fig 4b is showing the ZnO surface defect mediated PL bands (excitation: 325 nm) deconvoluted into two Gaussian components centered at 527 nm and 570 nm, respectively.

https://doi.org/10.1371/journal.pone.0189276.g004

the absorption edge into the visible region. The bandgap (Eg) of ZnO was found to be around 3.23 eV obtained by using tauc plot [65] as shown in Fig 4 (inset). Similar values of bandgap was also reported previously in literature [50,66]. The visible light absorption by ZnO nanostructures have been attributed due to the presence of native point defects in the crystal lattice of ZnO which reduce the energy required for exciton pair generation upon photo-excitation [67,68]. The visible light activity of ZnO with respect to the concentration of defect states is

also reported by Tang et al. [69] where they have demonstrated reduction in the optical band-gap of ZnO with increasing oxygen vacancy states.

In order to investigate the presence of defect states in the synthesized and annealed ZnO nanorods, we measured the photoluminescence (PL) spectrum of the nanorods. Fig 4(b) shows the room temperature steady state PL spectrum of ZnO nanorods measured with 325 nm monochromatic light. The PL spectrum exhibit three major peaks, where the absorption around 385 nm that can be attributed to the direct recombination of excited electrons from the conduction band (CB) to the valence band (VB) of the ZnO nanorods. The origin of the violet emission (at 420 nm) is attributed to the deep-level zinc interstitial (Zn_i) defects that are slightly below the CB of ZnO [70]. This emission occurs due to the capture of excited electrons from the CB of ZnO by Zn_i defect states through non-radiative transition followed by a radiative recombination of the electrons from the defect states to the VB. The broad emission in the range from 490 nm to 635 nm, which is found to compose of two Gaussian components centered at 527 nm and 570 nm respectively is mainly due to the surface situated oxygen vacancy states, where singly charged oxygen vacancies (V_O^+) are responsible for the 527 nm emission and the 570 nm emission originates from the oxygen vacancy states with doubly charged states (V_O^{++}) [67,71].

The VLP activity of the ZnO nanorods was then studied for BTEX removal in aqueous medium and detected by GC/MS (Supporting information S1 Fig). Fig 5 shows the degradation profile of the individual monoaromatic hydrocarbons (initial concentration: 25 ppm) in the presence and absence of ZnO nanorods under simulated solar irradiation. For 25 ppm benzene, in the absence of ZnO nanorods, negligible amount of benzene was found to degrade during 3 hours of visible light irradiation carried out in these experiments. On the contrary, in

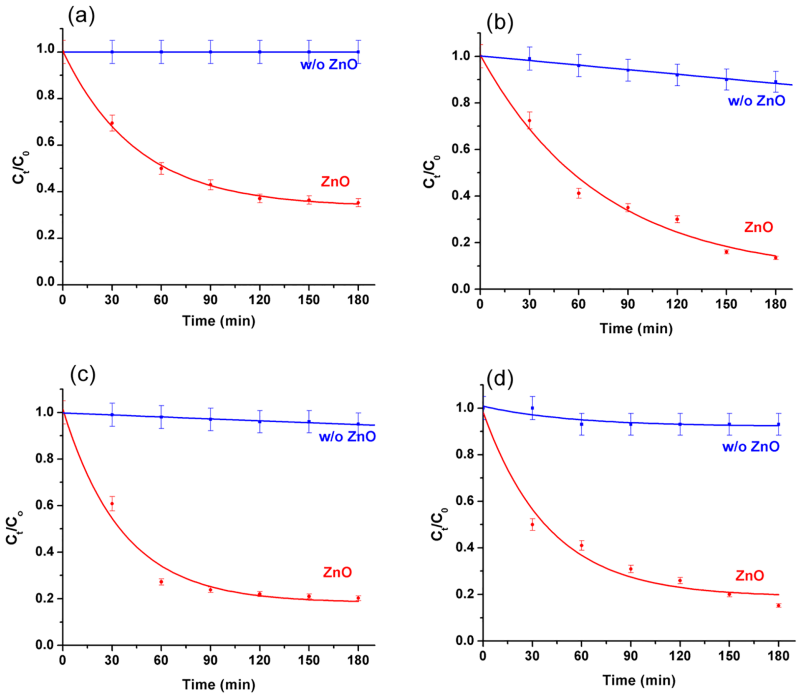

Fig 5. Reduction in the concentrations of (a) benzene, (b) toluene, (c) ethylbenzene and (d) xylene. Reduction in the concentration of (a) benzene, (b) toluene, (c) ethylbenzene and (d) xylene under simulated solar light irradiation (incident power: 1 kW/m^2) in the presence and absence of ZnO nanorods. The starting concentration of all the monoaromatic hydrocarbons was 25 ppm.

https://doi.org/10.1371/journal.pone.0189276.g005

the presence of ZnO nanorods, 50% degradation of benzene was observed in about 1 hour exhibiting almost 1.75 times higher degradation. Other three monoaromatic hydrocarbons (toluene, ethylbenzene and xylene) also showed similar degradation trends in the presence of ZnO nanorods. Based on the percentage removal of each monoaromatic hydrocarbons upon 3 hours of photocatalytic treatment, we found that both toluene and xylene were degraded almost equally by the ZnO nanorods exhibiting ~90% reduction in their concentrations within 3 hours, followed by ethylbenzene (~80%) and finally benzene (~65%). The instrumental detection limits of benzene, toluene, ethylbenzene and xylene by using GC/MS were tested and found 10, 5, 10 and 10 ppb (μg/L) respectively.

The photocatalytic degradation of BTEX as a function of initial concentration of the test contaminants in the presence of ZnO nanorods was then investigated by using Langmuir-Hinshelwood (L-H) kinetics model. The L-H model has been previously used for heterogeneous photocatalysis to explain the bimolecular reaction of two surface adsorbed species [72–74]. The model is mathematically given as:

$$\frac{1}{k_{obs}} = \frac{1}{k_c K_{LH}} + \frac{A_o}{k_c} \quad (1)$$

where A_o is the initial concentration of the test contaminant (in $mg.L^{-1}$), k_{obs} is the apparent pseudo-first-order rate constant, k_c is the rate constant of surface reaction (in $mg.L^{-1}.min^{-1}$) and K_{LH} is the Langmuir–Hinshelwood adsorption equilibrium constant (in $L.mg^{-1}$).

The initial concentration of each monoaromatic hydrocarbon of BTEX was varied from 10 to 100 ppm and the values of k_{obs} was determined for each initial concentrations using a first order exponential fitting to their photocatalytic degradation curves (as shown in Fig 5). In Fig 6 we have plotted 1/ k_{obs} vs. initial concentration of each monoaromatic hydrocarbon of BTEX

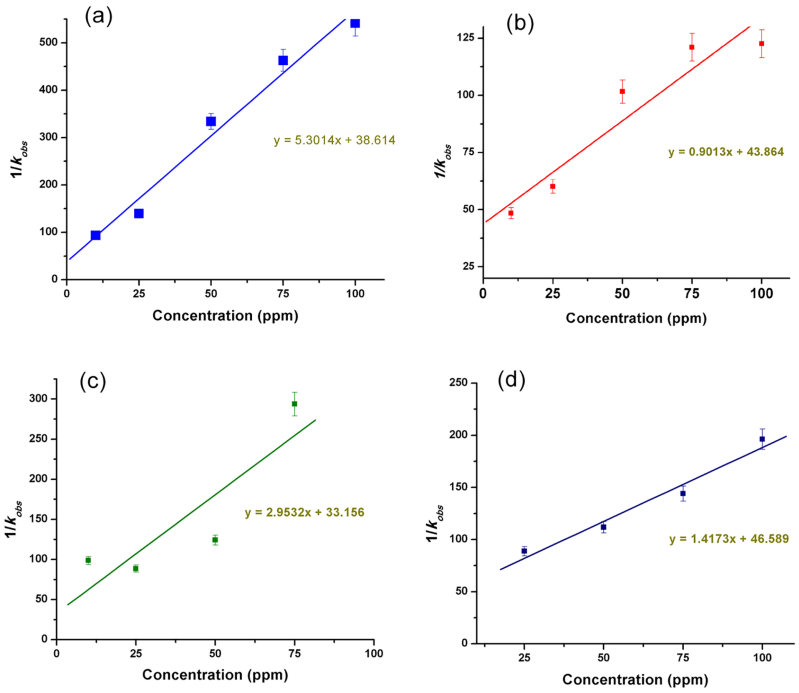

Fig 6. Plots representing the rate constants vs. initial concentrations of (a) benzene, (b) toluene, (c) ethylbenzene and (d) xylene.

https://doi.org/10.1371/journal.pone.0189276.g006

Table 1. Langmuir-Hinshelwood adsorption equilibrium constant (KLH) and rate constant for surface reaction (k_c) values of BTEX obtained when individual BTEX molecules were photocatalytically treated using supported zinc oxide nanorods under visible light irradiation.

Chemical	k_c	K_{LH}
	($mg.L^{-1}.min^{-1}$)	($L.mg^{-1}$)
Benzene	0.189	0.1373
Toluene	1.109	0.0205
Ethylbenzene	0.339	0.0891
Xylene	0.706	0.0304

https://doi.org/10.1371/journal.pone.0189276.t001

which shows a linear relationship between the initial concentration and 1/ k_{obs} confirming the L-H kinetic relationship [75,76]. The values of k_c and K_{LH} were then determined from the slope and Y-axis intersection of the linearly fitted line respectively, that are summarized in Table 1. Amongst the individual BTEX components, toluene shown maximum kc value of 1.109 $mg.L^{-1}.min^{-1}$ with lowest K_{LH} (0.0205 $L.mg^{-1}$) indicating maximum adsorption on the ZnO nanorod surface, followed by xylene, ethylbenzene and finally benzene. These observations clearly conform to our results on the photocatalytic degradation efficiency of the monoaromatic hydrocarbons of BTEX as shown in Fig 5.

The complete mineralization process of BTEX was investigated using a 25 ppm BTEX mixture solution in DI water to better understand the mineralization of BTEX. Using the HPLC technique, benzyl alcohol, benzaldehyde, phenol and benzoic acid were detected as intermediate byproducts that formed during the photocatalytic degradation of BTEX (Supporting information S2 Fig). Detailed investigation of the formation of intermediates and visible light

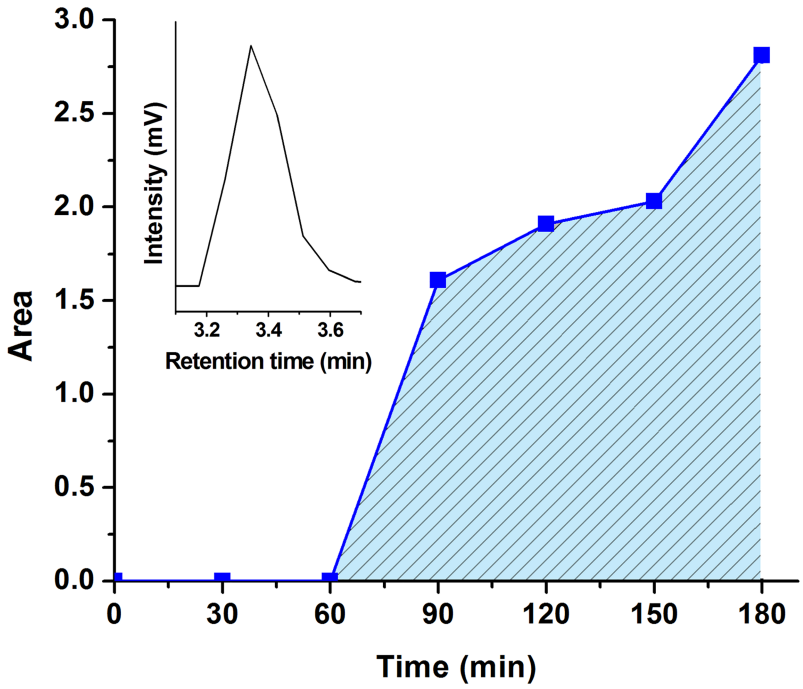

Fig 7. Evolution of carbon dioxide over time during BTEX photocatalytic degradation. Evolution of carbon dioxide over time degradation of 25 ppm BTEX mixture in DI water in the presence of ZnO nanorods under the simulated solar light irradiation as determined by using GC fitted with thermal conductivity detector (TCD). Inset shows the CO_2 chromatogram detected at retention time 3.34 minutes.

https://doi.org/10.1371/journal.pone.0189276.g007

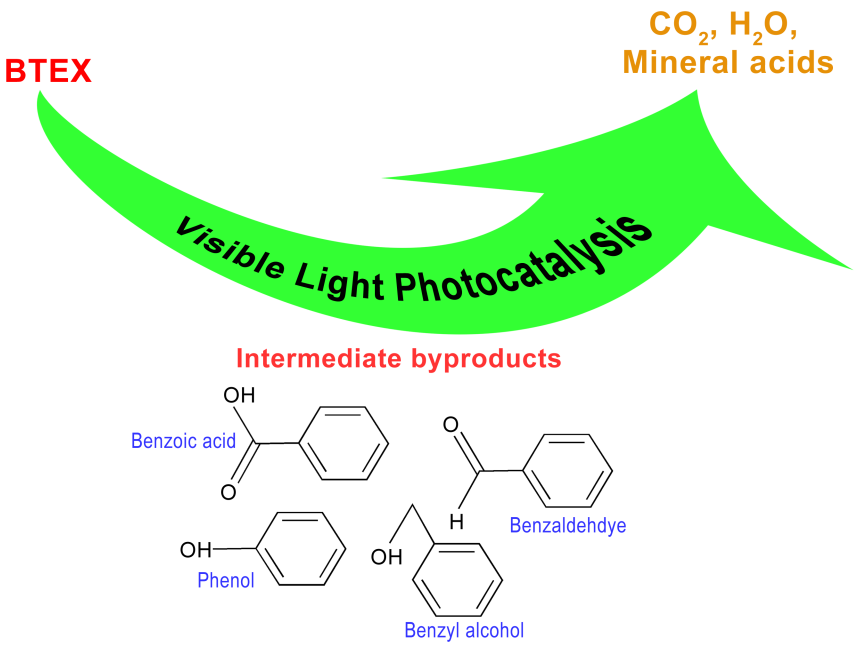

Fig 8. Schematic representation of visible light photocatalytic degradation of BTEX. Visible light photocatalytic degradation of BTEX in aqueous medium in the presence of ZnO nanorods as supported photocatalyst. Upon photo excitation, BTEX molecules are photocatalytically degraded by the ZnO nanorods resulting in various types of intermediate byproduct, which upon successive photo-oxidation produces CO_2, H_2O and mineral acids leading to the complete mineralization of BTEX.

https://doi.org/10.1371/journal.pone.0189276.g008

photocatalytic degradation pathway of BTEX is currently on going. Similar intermediate byproduct formation as a result of photocatalytic degradation of BTEX was also reported by several other researchers [56,77–80]. Production of CO_2 as a result of successive photo-oxidation of BTEX and the intermediate byproducts was detected after 1 hour of continuous photocatalytic degradation of BTEX with ZnO nanorods as shown in Fig 7, where CO_2 content was observed to increase continuously after 1 hour indicating complete mineralization of BTEX mainly into CO_2 and water. Based on these observations, the VLP degradation of BTEX with ZnO nanorods as a photocatalyst is schematically represented in Fig 8.

Conclusions

Microwave assisted hydrothermal process was used successfully to grow ZnO nanorods on glass support and used as supported visible light photocatalyst to degrade BTEX in aqueous medium. Presence of native point defects, mainly zinc interstitial and oxygen vacancy states extend the absorption edge of the ZnO nanorods into the visible region. As a result, efficient visible light photocatalytic (VLP) degradation of BTEX was observed in the presence of ZnO nanorods, resulting in almost 90% reduction in toluene and xylene concentrations as well as ~80% reduction in ethylbenzene and ~65% reduction in benzene within 3 hours. Langmuir-Hinshelwood kinetic model fits well with the experimental results showing a maximum reaction and adsorption/desorption equilibrium constants for toluene with the ZnO nanorod surface, followed by xylene, ethylbenzene and benzene, respectively. Further investigation of photocatalytic degradation of BTEX by ZnO nanorods as visible light photocatalyst exhibited formation of benzyl alcohol, benzaldehyde, phenol and benzoic acid as intermediate byproducts. CO_2 evolution as a result of successive photo-oxidation of BTEX and its intermediate

byproducts was also evaluated which was found to increase over time indicating the final mineralization of the BTEX molecules into benign products.

Supporting information

S1 Fig. GC/MS chromatogram of BTEX.
(DOCX)

S2 Fig. HPLC chromatogram of BTEX intermediate products.
(DOCX)

Acknowledgments

Authors would like to acknowledge financial and technical support from the Chair in Nanotechnology for Water Desalination, the Research Council (TRC) of Oman; College of Agricultural and Marine Sciences (Central instrument laboratory) and the Department of Petroleum and Chemical Engineering, College of Engineering, Sultan Qaboos University, Oman.

Author Contributions

Formal analysis: Jamal Al-Sabahi, Tanujjal Bora.

Methodology: Jamal Al-Sabahi, Tanujjal Bora.

Project administration: Mohammed Al-Abri.

Supervision: Mohammed Al-Abri, Joydeep Dutta.

Writing – original draft: Jamal Al-Sabahi, Tanujjal Bora.

Writing – review & editing: Mohammed Al-Abri, Joydeep Dutta.

References

1. Fernandez-Lima FA, Becker C, McKenna AM, Rodgers RP, Marshall AG, et al. (2009) Petroleum Crude Oil Characterization by IMS-MS and FTICR MS. Anal Chem 81: 9941–9947. https://doi.org/10.1021/ac901594f PMID: 19904990
2. Klein GC, Angström A, Rodgers RP, Marshall AG (2006) Use of Saturates/Aromatics/Resins/Asphaltenes (SARA) Fractionation To Determine Matrix Effects in Crude Oil Analysis by Electrospray Ionization Fourier Transform Ion Cyclotron Resonance Mass Spectrometry. Energy Fuels 20: 668–672.
3. Hughey CA, Rodgers RP, Marshall AG (2002) Resolution of 11 000 Compositionally Distinct Components in a Single Electrospray Ionization Fourier Transform Ion Cyclotron Resonance Mass Spectrum of Crude Oil. Anal Chem 74: 4145–4149. PMID: 12199586
4. Bamberger M, Oswald RE (2015) Long-term impacts of unconventional drilling operations on human and animal health. J Environ Sci Health, Part A 50: 447–459.
5. do Rego ECP, Pereira Netto AD (2007) PAHs and BTEX in Groundwater of Gasoline Stations from Rio de Janeiro City, Brazil. Bull of EnvironContam Toxicol 79: 660–664.
6. Osborn SG, Vengosh A, Warner NR, Jackson RB. Methane contamination of drinking water accompanying gas-well drilling and hydraulic fracturing; 2011; USA. pp. 8172–8176.
7. Dórea HS, Bispo JRL, Aragão KAS, Cunha BB, Navickiene S, et al. (2007) Analysis of BTEX, PAHs and metals in the oilfield produced water in the State of Sergipe, Brazil. Microchem J 85: 234–238.
8. Ishak S, Malakahmad A, Isa MH (2012) Refinery wastewater biological treatment: A short review. J Sci Ind Res 71: 251–256.
9. Fakhru'l-Razi A, Pendashteh A, Abdullah LC, Biak DRA, Madaeni SS, et al. (2009) Review of technologies for oil and gas produced water treatment. J Hazard Mater 170: 530–551. https://doi.org/10.1016/j.jhazmat.2009.05.044 PMID: 19505758

10. Li H, Son JH, Carlson KH (2016) Concurrence of aqueous and gas phase contamination of groundwater in the Wattenberg oil and gas field of northern Colorado. Water Res 88: 458–466. https://doi.org/10.1016/j.watres.2015.10.031 PMID: 26519629
11. Colborn T, Kwiatkowski C, Schultz K, Bachran M (2011) Natural gas operations from a public health perspective. Hum and Ecol Risk Assess 17: 1039–1056.
12. Voice TC, Pak D, Zhao X, Shi J, Hickey RF (1992) Biological activated carbon in fluidized bed reactors for the treatment of groundwater contaminated with volatile aromatic hydrocarbons. Water Res 26: 1389–1401.
13. Hickey RF, Wagner D, Mazewski G (1990) Combined biological fluid bed-carbon adsorption system for BTEX contaminated ground-water remediation. Fourth National Outdoor Action Conference on Aquifer Restoration, Groundwater Monitoring and Geophysical Methods. Las Vegas, NV, USA.
14. Allen EW (2008) Process water treatment in Canada's oil sands industry: II. A review of emerging technologies. J Environ Eng Sci 7: 499–524.
15. Coelho A, Castro AV, Dezotti M, Sant'Anna GL Jr (2006) Treatment of petroleum refinery sourwater by advanced oxidation processes. J Hazard Mater 137: 178–184. https://doi.org/10.1016/j.jhazmat.2006.01.051 PMID: 16530949
16. Tiburtius ERL, Peralta-Zamora P, Emmel A (2005) Treatment of gasoline-contaminated waters by advanced oxidation processes. J Hazard Mater 126: 86–90. https://doi.org/10.1016/j.jhazmat.2005.06.003 PMID: 16051429
17. Munter R. Advanced oxidation processes-current status and prospects. In: Aben H, editor; 2001; Tallinn, Estonia. Estonian Academy of Sciences. pp. 59–80.
18. Mandal T, Maity S, Dasgupta D, Datta S (2010) Advanced oxidation process and biotreatment: Their roles in combined industrial wastewater treatment. Desalin 250: 87–94.
19. Wang JL, Xu LJ (2012) Advanced Oxidation Processes for Wastewater Treatment: Formation of Hydroxyl Radical and Application. Crit Rev Environ Sci Technol 42: 251–325.
20. Fulekar MH, Pathak B, Kale RK (2014) Nanotechnology: Perspective for Environmental Sustainability. In: Fulekar MH, Pathak B, Kale RK, editors. Environ Sustainable Dev. New Delhi: Springer. pp. 87–114.
21. Tao Y, Cheng ZL, Ting KE, Yin XJ (2012) Photocatalytic Degradation of Phenol Using a Nanocatalyst: The Mechanism and Kinetics. J Catal 2013: 1–6.
22. Mahmood MA, Baruah S, Anal AK, Dutta J (2012) Heterogeneous photocatalysis for removal of microbes from water. Environ Chem Lett 10: 145–151.
23. Lazar M, Varghese S, Nair S (2012) Photocatalytic Water Treatment by Titanium Dioxide: Recent Updates. Catal 2: 572.
24. Gaya UI, Abdullah AH (2008) Heterogeneous photocatalytic degradation of organic contaminants over titanium dioxide: A review of fundamentals, progress and problems. J Photochem Photobiol, C 9: 1–12.
25. Chakrabarti S, Dutta BK (2004) Photocatalytic degradation of model textile dyes in wastewater using ZnO as semiconductor catalyst. J Hazard Mater 112: 269–278. https://doi.org/10.1016/j.jhazmat.2004.05.013 PMID: 15302448
26. Tripathi KM, Tran TS, Kim YJ, Kim T (2017) Green Fluorescent Onion-Like Carbon Nanoparticles from Flaxseed Oil for Visible Light Induced Photocatalytic Applications and Label-Free Detection of Al (III) Ions. ACS Sustainable Chemistry & Engineering 5: 3982–3992.
27. Tyagi A, Tripathi KM, Singh N, Choudhary S, Gupta RK (2016) Green synthesis of carbon quantum dots from lemon peel waste: applications in sensing and photocatalysis. RSC Advances 6: 72423–72432.
28. Jing Y-Q, Gui C-X, Qu J, Hao S-M, Wang Q-Q, et al. (2017) Silver silicate@ carbon nanotube nanocomposites for enhanced visible light photodegradation performance. ACS Sustainable Chemistry & Engineering 5: 3641–3649.
29. Hagfeldt A, & Graetzel M. (1995) Light-induced redox reactions in nanocrystalline systems. Chem Rev 95: 49–68.
30. Zhang H, Chen G., & Bahnemann D. W. (2009) Photoelectrocatalytic materials for environmental applications. J Mater Chem 19: 5089–5121.
31. Yoon TP, Ischay MA, Du J (2010) Visible light photocatalysis as a greener approach to photochemical synthesis. Nat Chem 2: 527–532. https://doi.org/10.1038/nchem.687 PMID: 20571569
32. Yuan Z, Jiaqiang X, Pengcheng X, Yongheng Z, Xuedong C, et al. (2010) Decoration of ZnO nanowires with Pt nanoparticles and their improved gas sensing and photocatalytic performance. Nanotechnol 21: 285501.

33. Bora T, Kyaw HH, Sarkar S, Pal SK, Dutta J (2011) Highly efficient ZnO/Au Schottky barrier dye-sensitized solar cells: Role of gold nanoparticles on the charge-transfer process. Beilstein J Nanotechnol 2: 681–690. https://doi.org/10.3762/bjnano.2.73 PMID: 22043457

34. Zhao Z, Song J-L, Zheng J-H, Lian J-S (2014) Optical properties and photocatalytic activity of Nd-doped ZnO powders. Trans Nonferrous Met Soc China 24: 1434–1439.

35. Ullah R, Dutta J (2007) Synthesis and Optical Properties of Transition Metal Doped ZnO Nanoparticles. International Conference on Emerging Technologies, ICET 2007. Islamabad, Pakistan. pp. 306–311.

36. Najam Khan M, Al-Hinai M, Al-Hinai A, Dutta J (2014) Visible light photocatalysis of mixed phase zinc stannate/zinc oxide nanostructures precipitated at room temperature in aqueous media. Ceram Int 40: 8743–8752.

37. Danwittayakul S, Jaisai M, Dutta J (2015) Efficient solar photocatalytic degradation of textile wastewater using ZnO/ZTO composites. Appl Catal, B 163: 1–8.

38. Vinoth R, Karthik P., Devan K., Neppolian B., & Ashokkumar M. (2017) TiO 2–NiO p–n nanocomposite with enhanced sonophotocatalytic activity under diffused sunlight. Ultrason Sonochem 35: 655–663. https://doi.org/10.1016/j.ultsonch.2016.03.005 PMID: 26968646

39. Raizada P, Shandilya P., Singh P., & Thakur P. (2016) Solar light-facilitated oxytetracycline removal from the aqueous phase utilizing a H 2 O 2/ZnWO 4/CaO catalytic system. J Taibah Univ Sci: 1–11.

40. Liu S, Li C, Yu J, Xiang Q (2011) Improved visible-light photocatalytic activity of porous carbon self-doped ZnO nanosheet-assembled flowers. CrystEngComm 13: 2533–2541.

41. Al-Sabahi J, Bora T, Al-Abri M, Dutta J (2016) Controlled Defects of Zinc Oxide Nanorods for Efficient Visible Light Photocatalytic Degradation of Phenol. Mater 9: 238.

42. Chen D, Wang Z, Ren T, Ding H, Yao W, et al. (2014) Influence of Defects on the Photocatalytic Activity of ZnO. J Phys ChemC 118: 15300–15307.

43. Fang J, Fan H, Ma Y, Wang Z, Chang Q (2015) Surface defects control for ZnO nanorods synthesized by quenching and their anti-recombination in photocatalysis. Appl Surf Sci 332: 47–54.

44. Baruah S, Rafique RF, Dutta J (2008) Visible light photocatalysis by tailoring crystal defects in zinc oxide nanostructures. Nanotechnol 3: 399–407.

45. Wahab R, Siddiqui MA, Saquib Q, Dwivedi S, Ahmad J, et al. (2014) ZnO nanoparticles induced oxidative stress and apoptosis in HepG2 and MCF-7 cancer cells and their antibacterial activity. Colloids and surfaces B: Biointerfaces 117: 267–276. https://doi.org/10.1016/j.colsurfb.2014.02.038 PMID: 24657613

46. Wahab R, Kaushik N, Khan F, Kaushik NK, Choi EH, et al. (2016) Self-Styled ZnO Nanostructures Promotes the cancer cell damage and supresses the epithelial phenotype of Glioblastoma. Scientific reports 6.

47. Das D, Datta AK, Kumbhakar DV, Ghosh B, Pramanik A, et al. (2017) Assessment of photocatalytic potentiality and determination of ecotoxicity (using plant model for better environmental applicability) of synthesized copper, copper oxide and copper-doped zinc oxide nanoparticles. PloS one 12: e0182823. https://doi.org/10.1371/journal.pone.0182823 PMID: 28796823

48. Reimer T, Paulowicz I, Röder R, Kaps Sr, Lupan O, et al. (2014) Single step integration of ZnO nano- and microneedles in Si trenches by novel flame transport approach: whispering gallery modes and photocatalytic properties. ACS applied materials & interfaces 6: 7806–7815.

49. Mishra YK, Modi G, Cretu V, Postica V, Lupan O, et al. (2015) Direct growth of freestanding ZnO tetrapod networks for multifunctional applications in photocatalysis, UV photodetection, and gas sensing. ACS applied materials & interfaces 7: 14303–14316.

50. Meenakshi G, Sivasamy A (2017) Synthesis and characterization of zinc oxide nanorods and its photocatalytic activities towards degradation of 2, 4-D. Ecotoxicology and environmental safety 135: 243–251. https://doi.org/10.1016/j.ecoenv.2016.10.010 PMID: 27744194

51. Wahab R, Khan F, Mishra YK, Musarrat J, Al-Khedhairy AA (2016) Antibacterial studies and statistical design set data of quasi zinc oxide nanostructures. RSC Advances 6: 32328–32339.

52. Sathe P, Richter J, Myint MTZ, Dobretsov S, Dutta J (2016) Self-decontaminating photocatalytic zinc oxide nanorod coatings for prevention of marine microfouling: a mesocosm study. Biofouling 32: 383–395. https://doi.org/10.1080/08927014.2016.1146256 PMID: 26930216

53. Jabeen M, Iqbal MA, Kumar RV, Ahmed M, Javed MT (2013) Chemical synthesis of zinc oxide nanorods for enhanced hydrogen gas sensing. Chinese Physics B 23: 018504.

54. Mishra YK, Kaps S, Schuchardt A, Paulowicz I, Jin X, et al. (2013) Fabrication of macroscopically flexible and highly porous 3D semiconductor networks from interpenetrating nanostructures by a simple flame transport approach. Particle & Particle Systems Characterization 30: 775–783.

55. Singh P, Borthakur A, Srivastava N, Singh R, Tiwary D, et al. (2016) Photocatalytic Degradation of Benzene and Toluene in Aqueous Medium. Pollut 2: 199–210.

56. Goto T, Ogawa M (2016) Efficient photocatalytic oxidation of benzene to phenol by metal complex-clay/TiO2 hybrid photocatalyst. RSC Adv 6: 23794–23797.

57. Soltani T, & Lee B. K. (2017) Comparison of benzene and toluene photodegradation under visible light irradiation by Ba-doped BiFeO 3 magnetic nanoparticles with fast sonochemical synthesis. Photochemical & Photobiological Sciences. Photochem Photobiol Sci 16: 86–95.

58. Baruah S, Mahmood MA, Myint MTZ, Bora T, Dutta J (2010) Enhanced visible light photocatalysis through fast crystallization of zinc oxide nanorods. Beilstein J Nanotechnol 1: 14–20. https://doi.org/10.3762/bjnano.1.3 PMID: 21977391

59. Baruah S, Dutta J (2009) Hydrothermal growth of ZnO nanostructures. Sci Technol Adv Mater 10: 013001. https://doi.org/10.1088/1468-6996/10/1/013001 PMID: 27877250

60. Baruah S, Dutta J (2009) pH-dependent growth of zinc oxide nanorods. J Cryst Growth 311: 2549–2554.

61. Umang VD, Chengkun X, Jiamin W, Di G (2012) Solid-state dye-sensitized solar cells based on ordered ZnO nanowire arrays. Nanotechnol 23: 205401.

62. Foo KL, Hashim U, Muhammad K, Voon CH (2014) Sol–gel synthesized zinc oxide nanorods and their structural and optical investigation for optoelectronic application. Nanoscale Res Lett 9: 429–429. https://doi.org/10.1186/1556-276X-9-429 PMID: 25221458

63. Wang M, Ren F, Zhou J, Cai G, Cai L, et al. (2015) N doping to ZnO nanorods for photoelectrochemical water splitting under visible light: engineered impurity distribution and terraced band structure. Scientific reports 5.

64. Saoud K, Alsoubaihi R, Bensalah N, Bora T, Bertino M, et al. (2015) Synthesis of supported silver nanospheres on zinc oxide nanorods for visible light photocatalytic applications. Materials Research Bulletin 63: 134–140.

65. Mohan R, Drbohlavova J, Hubalek J (2013) Water-dispersible TiO2 nanoparticles via a biphasic solvothermal reaction method. Nanoscale research letters 8: 503. https://doi.org/10.1186/1556-276X-8-503 PMID: 24289214

66. Sáenz-Trevizo A, Amézaga-Madrid P, Pizá-Ruiz P, Antúnez-Flores W, Miki-Yoshida M (2016) Optical Band Gap Estimation of ZnO Nanorods. Materials Research 19: 33–38.

67. Janotti A, Van de Walle CG (2007) Native point defects in ZnO. Phys Rev B: Condens Matter 76: 165202.

68. Appavoo K, Liu M., & Sfeir M. Y. (2014) Role of size and defects in ultrafast broadband emission dynamics of ZnO nanostructures. Appl Phys Lett 104: 133101.

69. Tang Y, Zhou H, Zhang K, Ding J, Fan T, et al. (2015) Visible-light-active ZnO via oxygen vacancy manipulation for efficient formaldehyde photodegradation. Chem Eng J 262: 260–267.

70. Kang D, Liu A, Bian J, Sang Y (2012) Optoelectronic characteristics of zinc oxide nanorods/P3HT hybrid junctions investigated using surface photovoltage method. ECS Solid State Lett 1: 15–17.

71. Ye JD, Gu SL, Qin F, Zhu SM, Liu SM, et al. (2005) Correlation between green luminescence and morphology evolution of ZnO films. Appl Phys A 81: 759–762.

72. Saien J, Khezrianjoo S (2008) Degradation of the fungicide carbendazim in aqueous solutions with UV/TiO2 process: Optimization, kinetics and toxicity studies. J Hazard Mater 157: 269–276. https://doi.org/10.1016/j.jhazmat.2007.12.094 PMID: 18243543

73. Vasanth Kumar K, Porkodi K, Selvaganapathi A (2007) Constrain in solving Langmuir–Hinshelwood kinetic expression for the photocatalytic degradation of Auramine O aqueous solutions by ZnO catalyst. Dyes Pigm 75: 246–249.

74. Krishnakumar B, Swaminathan M (2011) Influence of operational parameters on photocatalytic degradation of a genotoxic azo dye Acid Violet 7 in aqueous ZnO suspensions. Spectrochim Acta, Part A 81: 739–744.

75. Khezrianjoo S, Revanasiddappa HD (2012) Langmuir-Hinshelwood kinetic expression for the photocatalytic degradation of Metanil Yellow aqueous solutions by ZnO catalyst. Chem Sci J 3: 1–7.

76. Kumar KV, Porkodi K, Rocha F (2008) Langmuir–Hinshelwood kinetics—A theoretical study. Catal Commun 9: 82–84.

77. Park J-H, Seo Y-S, Kim H-S, Kim I-K (2011) Photodegradation of benzene, toluene, ethylbenzene and xylene by fluidized bed gaseous reactor with TiO2/SiO2 photocatalysts. Korean J Chem Eng 28: 1693–1697.

78. Ardizzone S, Bianchi CL, Cappelletti G, Naldoni A, Pirola C (2008) Photocatalytic Degradation of Toluene in the Gas Phase: Relationship between Surface Species and Catalyst Features. Environ Sci Technol 42: 6671–6676. PMID: 18800547

79. Mao Y, Bakac A (1996) Photocatalytic Oxidation of Toluene to Benzaldehyde by Molecular Oxygen. J Phys Chem 100: 4219–4223.

80. d'Hennezel O, Pichat P, Ollis DF (1998) Benzene and toluene gas-phase photocatalytic degradation over H 2 O and HCL pretreated TiO 2: by-products and mechanisms. J Photochem Photobiol, A 118: 197–204.